

Passive Neutron Multiplicity Device for ^{240}Pu Measurement Based on FPGA*

Yan Zhang,^{1,2,†} Hao-Ran Zhang,^{1,2} Ren-Bo Wang,^{1,2,3} Ming-Yu Li,³ Rui Chen,²
Hai-Tao Wang,^{1,2} Xiang-Ting Meng,² Shu-Min Zhou,^{2,‡} and Bin Tang^{1,2,§}

¹Fundamental Science on Radioactive Geology and Exploration Technology Laboratory,
East China University of Technology, Nanchang 330013, China

²Engineering Research Center for Nuclear Technology Application,
Ministry of Education, East China University of Technology, Nanchang 330013, China

³Pan China Detect Technology Co. Ltd., Nanchang 330013, China

A passive neutron multiplicity measurement device, FH-NCM/S1, based on field-programmable gate arrays (FPGAs), is developed specifically for measuring the mass of plutonium-240 (^{240}Pu) in mixed oxide fuel. FH-NCM/S1 adopts an integrated approach, combining the shift-register analysis mode with the pulse-position timestamp mode using an FPGA. The optimal effective length of the ^3He neutron detector was determined to be 30 cm, and the thickness of the graphite reflector was ascertained to be 15 cm through MCNP simulations. After fabricating the device, calibration measurements were performed using a ^{252}Cf neutron source; a detection efficiency of 43.07 % and detector die-away time of 55.79 μs were observed. Nine samples of plutonium oxide were measured under identical conditions using the FH-NCM/S1 in shift-register analysis mode and a plutonium-waste multiplicity counter. The obtained double rates underwent corrections for detection efficiency (ϵ) and double gate fraction (f_d), resulting in corrected double rates (D_c), which were used to validate the accuracy of the shift-register analysis mode. Furthermore, the device exhibited fluctuations in the measurement results, and within a single 20-s measurement, these fluctuations remained below 10 %. After 30 cycles, the relative error in the mass of ^{240}Pu was less than 5 %. Finally, correlation calculations confirmed the robust consistency of both measurement modes. This study holds specific significance for the subsequent design and development of neutron multiplicity devices.

Keywords: Spent fuel, Non-destructive assay, Neutron multiplicity, ^{240}Pu , FPGA

I. INTRODUCTION

Mixed oxide (MOX) fuel constitutes approximately 5 % of the global inventory of light-water reactor fuel, with an annual utilization rate of approximately 2000 tons. Forecasts suggest that MOX fuel is likely to play a pivotal role in breeder reactor initiatives globally. The uranium/plutonium equilibrium within MOX fuel is a pivotal parameter that requires meticulous scrutiny. Both the uranium and plutonium compositions within the fuel and segregated uranium and plutonium constituents must be determined to achieve a comprehensive and closed uranium/plutonium mass equilibrium [24–26].

Nondestructive assay (NDA) methodologies and apparatuses for determining uranium and plutonium contents represent a focal point in nuclear-fuel assessment. This involves the utilization of techniques, such as detecting uranium and plutonium isotope-decay processes, particularly through the observation of γ radiation emanating from nuclear fuel [5, 6, 9]. For example, Canberra's Tomographic Gamma Scanner (TGS) is a representative product [8] capable of providing comprehensive quantitative gamma analy-

sis for fissile materials or transuranic radionuclides. However, its applicability is constrained by factors such as prolonged measurement duration, intricacies in equipment operation, associated costs, specialized skill requirements, and the exclusive focus on evaluating plutonium quality in minute uranium-plutonium amalgams or plutonium oxides, rendering this methodology prohibitively expensive.

Quantifying plutonium content based solely on γ -ray [27] intensity is compromised by the inherent self-absorption tendencies of the sample. Notably, uranium and plutonium isotopes not only emit γ rays, but also exhibit pronounced multiplicity [1–3] characteristics through the release of robust spontaneous fission neutrons. Capitalizing on this principle, the High-Level Neutron Coincidence Counter was developed in 1979 by the Los Alamos National Laboratory (LANL) in the United States to gauge substantial plutonium samples. The methodology was adopted by the International Atomic Energy Agency for global plutonium material accounting [4].

Canberra innovatively introduced a suite of products based on the spontaneous fission of ^{240}Pu and the concurrent emission of multiple fast neutrons. These products leverage three-ring, four-ring, and five-ring multiple neutron detectors for coincident measurements, achieving a detection limit of less than 10 nCi/g with a sample volume of 208 L.

In 2009, the Chinese Academy of Atomic Energy Sciences pioneered the development of a neutron-measurement apparatus for nuclear waste encapsulated in drums. This device quantified the mass of Pu by assessing the neutrons generated through spontaneous fission. Remarkably, the detection efficiency of the device was 30.6 %, with a lower limit of detection below 100 mg of the effective mass of ^{240}Pu .

Owing to the scarcity of ^3He gas, the focal point of in-

* This work was supported by the National Natural Science Foundation of China (NO. 42374226), Natural Science Foundation of Jiangxi Province (NO. 20232BAB201043 and 20232BCJ23006), a sub-project of the nuclear-energy development project of the China National Defense Science and Industry Bureau 'n- γ fusion logging method theory research' (Grant No.20201192-01), and the Fundamental Science on Radioactive Geology and Exploration Technology Laboratory (2022RGET20).

† Corresponding author, Yan Zhang, yanzhang@ecut.edu.cn.

‡ Corresponding author, Shu-Min Zhou, smzhou@ecut.edu.cn.

§ Corresponding author, Bin Tang, tangbin@ecit.cn.

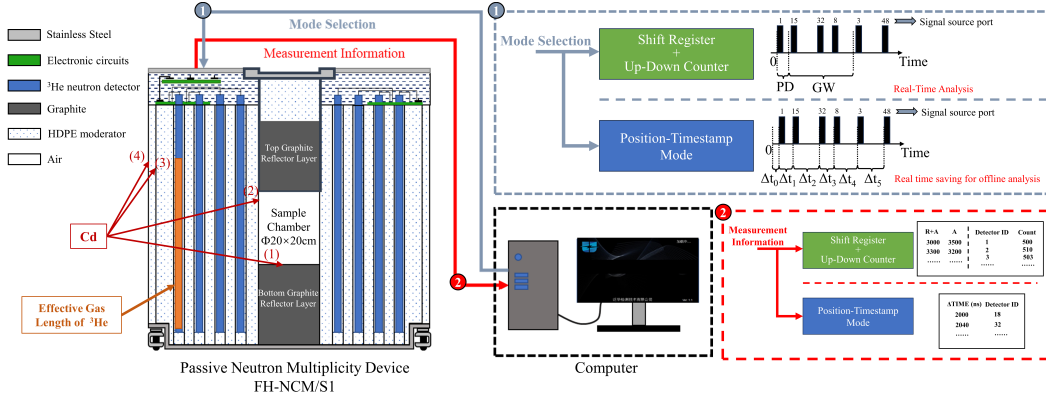


Fig. 1. Diagram of FH-NCM/S1 passive neutron multiplicity device.

strumental research and development (R&D) underwent a paradigm shift towards innovation in novel neutron detectors post-2010. Multiple R&D teams in cognate domains have pioneered the development of a suite of coincidence measurement and multiplicity devices. These innovations are based on boron-coated proportional counters [17], liquid scintillator detectors, and LiF/ZnS-based scintillator neutron coincidence counters [20]. However, these advancements are accompanied by challenges, such as suboptimal detection efficiency [5] and protracted neutron decay times, necessitating extended measurement durations to ensure the precision of each assessment [20, 22, 23]. Therefore, despite these endeavors, ^3He neutron detectors are preferred for applications within the industrial sphere.

Two methodologies are currently dominant in the field of data processing across various devices. The first is based on shift registers, as exemplified by the JSR-15 Handheld Multiplicity Register crafted by the LANL. However, data acquisition entails the amalgamation of data outputs in list mode, a paradigm embodied by the Advanced List Mode [15] Multiplicity Module [19], also manufactured by the LANL.

This study investigates the requirements for a nondestructive assay (NDA) of ^{240}Pu quality in MOX fuel, presenting the conceptualization, assembly, and evaluation of an innovative plutonium quality-assessment apparatus, FH-NCM/S1. To optimize the instrument cost while adhering to the user-specified technical parameters, a Monte Carlo simulation is employed to determine the effective length of the primary component, ^3He , and dimensions of the graphite reflector layer.

In pursuit of diversity in analysis circuits, a holistic strategy is adopted by integrating the multiplicity register with the list-mode multiplicity method using field-programmable gate arrays (FPGAs). This approach offers users an expansive array of data-acquisition methods. Each ^3He neutron detector is accompanied by a preamplifier circuit, wherein the nuclear signal generated undergoes amplification and shaping and is transformed into a square-wave signal with a pulse width ranging from 2 to 3 microseconds. After scanning the

pulse signal via the FPGA, the multichannel outcomes are consolidated into a singular digital signal after noise reduction.

The FH-NCM/S1 is designed for ^{240}Pu -quality measurement and underwent rigorous analysis through experimental assessments using a ^{252}Cf neutron source and standard samples. The rationality and precision of the instrument are authenticated by cross-referencing measurements of identical standard samples using a traditional plutonium scrap multiplicity counter (PSMC).

II. DEVICE DESIGN OPTIMIZATION AND RELATED PARAMETER INDICATORS

A. Overall Design of the Device

The passive neutron multiplicity measurement device consists of a relatively fixed structure, including a sample chamber, top- and bottom-end plugs, neutron detectors, moderators, and electronic circuits. Fig. 1 shows a schematic of the passive neutron multiplicity measurement device designed to measure the mass of ^{240}Pu in special materials, named FH-NCM/S1.

The left-hand side of Fig. 1 outlines the primary structure of the device. The sample chamber is positioned at the center and adheres to the design specifications, which assume a cylindrical configuration with a bottom diameter of 20 cm and height of 20 cm. Two end plugs primarily composed of graphite were placed at the top and bottom of the sample cavity. These end plugs served as reflective layers that decreased the escape of fast neutrons generated by sample fission from the axial direction of the sample cavity. The ^3He neutron-detector array system is shown in blue. This array was arranged in high-density polyethylene in four concentric rings according to a predetermined pattern to detect spontaneous fission neutrons within the sample.

The overall detection efficiency of the device is a crucial indicator of its design process. Both the effective length of ^3He in the detector and the thickness of the graphite reflector

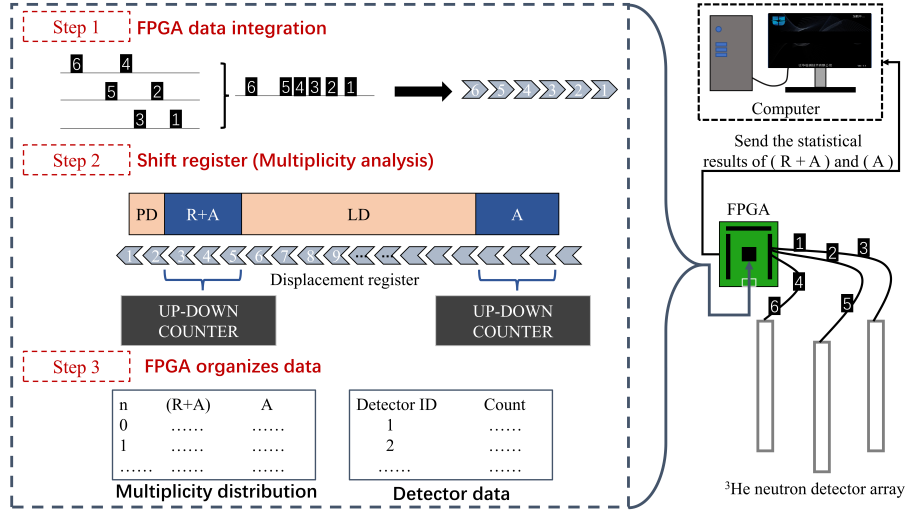


Fig. 2. FPGA signal acquisition and analysis process (shift-register analysis mode).

layer on the top plug play pivotal roles in determining this efficiency. Monte Carlo software simulations are subsequently used to establish these parameters, ensuring that the device design meets the criterion of detection efficiency exceeding 40 %, while also reflecting its economic feasibility.

To prevent the diffusion of thermal neutrons back into the sample chamber, a 1-mm-thick cadmium layer was incorporated on the exterior of the sample chamber to absorb thermal neutrons, as illustrated in Fig. 1 (1) and (2). Additionally, 1-mm-thick cadmium layers were implemented on the outer side of the inner slowing-down body and on the inner side of the second slowing-down body. The cadmium layer on the outer side of the inner slowing-down body absorbs thermal neutrons leaking from the sample that are undetected by the detector, as depicted in Fig. 1 (3). Moreover, the cadmium layer on the inner side of the second slowing-down body absorbs thermal neutrons entering the device from the outside, thereby reducing the impact of the environmental neutron background on the device performance, as shown in Fig. 1 (4).

The signal acquisition, analysis, and processing module of the FH-NCM/S1 is executed through an FPGA-based embedded system capable of enabling high-speed digital signal processing and communication functionalities. A 50-MHz clock crystal oscillator ensured a measurement-time accuracy of 20 ns. The device incorporates both the shift-register analysis mode (signal analysis and processing are completed through the shift registers and up-down counters), as illustrated by the green block in Fig. 1, and the list mode (referred to as the pulse-position timestamp mode in the text), depicted by the blue block in Fig. 1. Users have the flexibility to choose a suitable measurement method through the software interface, enabling the device to adapt to diverse measurement scenarios.

The traditional shift-register analysis mode consolidates multiple signals into a unified form, channeling the digital signal generated by the pulse time series into a shift register.

The distributions of R+A (real count and accidental count) and A (accidental count), which are crucial for multiplicity analysis, are derived by sequentially inputting the digital signal into distinct shift registers, such as the pre-delay time, coincidence gate width (or gate width), and long delay time, while regulating the output. For ease of portability, the signals from the eight ³He neutron detectors are typically amalgamated into a singular signal via an OR gate [4] and subsequently routed to JSR-15 for analysis.

However, in the design of FH-NCM/S1, careful consideration is given to the self-check predicament inherent in the detectors. The device employs an FPGA to directly scan 80 signals from the ³He neutron detector, enabling multichannel signal acquisition and simultaneous recording of the origin of the signal (ID of the detector). The analysis method is shown in the green block in Fig. 1.

The FPGA now encompasses the pulse-position timestamp mode, enabling not only direct industrial multiplicity analysis by the shift-register analysis mode, but also providing intricate pulse-time information. The output mode of Δt_n , representing the time interval between two recorded pulses in the pulse-position timestamp mode, is more suitable for jitter filtering and noise removal. Simultaneously, this mode can retain the original signal-measurement content for subsequent viewing and offline analysis. The output result is illustrated in step 2 of Fig. 1.

B. Principle of FPGA Signal Acquisition and Analysis

In the shift-register analysis mode, the front end of the data-acquisition and analysis device comprises several OR gate circuits. These circuits primarily eliminate randomization from multiple signals, consolidate them into a unified output, and facilitate subsequent connections with the acquisition and analysis device. However, this processing method requires a high level of consistency in the output-pulse signal

from each ^3He neutron detector and does not log the origin of the pulse signal (i.e., which ^3He neutron detector generates the signal). This poses a challenge in identifying and addressing the issues related to the failure of ^3He neutron detectors.

To overcome this limitation, the signal-acquisition and transmission module of FH-NCM/S1 adopts a direct connection method. The output signal of the ^3He neutron detector is directly linked to the FPGA pins, enabling the scanning and collection of all the pulses generated by the detectors. In this process, the analog pulse signal from the ^3He neutron detector undergoes preamplification, shaping, and amplification with a determined amplitude threshold. The resulting digital pulse signal is then directly fed into a digital-processing chip FPGA, where the pulse is recorded. The FPGA precisely records the position (Detector ID) and time of the acquired pulse front, ensuring a minimum resolution of 20 ns.

Regarding the analysis principle, FPGA functions are based on the acquisition method of traditional multiple-shift registers. The pulse time-stamp captures the collected signal as a time series, subsequently inputting it sequentially into the corresponding "coincidence" gate for shifting (as depicted in step 1). Within both the (R+A) and A gates, an up-down counter is programmed to record the data in real time in the gate (as illustrated in step 2). Upon completion of the data-shifting process, the results recorded by the reversible counters in the (R+A) gate and the A gate are the output (as indicated in step 3). A visual representation of the FPGA setup is shown in Fig. 2.

The FPGA accumulates statistical information from the (R+A) and A gates, which is then transmitted to the host computer. The host-computer software calculates the single/double/triple rate ($S/D/T$) using Eq. 1, Eq. 2, and Eq. 3 in subsequent analysis. The distribution in the (R+A) gate is denoted as $P(n)$, the distribution in the A gate is denoted as $Q(n)$, and 't' represents the measurement time [4].

$$S = \frac{\sum_{n=0}^{\max} P_n}{t} \quad (1)$$

$$D = \frac{\sum_{n=1}^{\max} nP_n - \sum_{n=1}^{\max} nQ_n}{t} \quad (2)$$

$$T = \frac{\sum_{n=2}^{\max} \frac{n(n-1)}{2} P_n - \sum_{n=2}^{\max} \frac{n(n-1)}{2} Q_n}{t} - \frac{(\sum_{n=1}^{\max} nQ_n)(\sum_{n=1}^{\max} nP_n - \sum_{n=1}^{\max} nQ_n)}{\sum_{n=0}^{\max} Q_n} \quad (3)$$

Furthermore, based on Eq. 1 and Eq. 2, the single rate represents the total neutron counting rate detected by the detector array, whereas the double rate represents the real count rate, that is, the coincident count rate. Compared to S, D more accurately reflects the rationality of the algorithms used in the device and the variations in various setup parameters. Therefore, it is often employed as a benchmark to analyze the rationality of a device.

In addition to the direct output of (R+A) and distribution of A, the shift-register analysis mode can be switched to the position timestamp mode using the host computer software. The Δt value between adjacent pulse signals can be directly output and subsequently integrated into a comprehensive pulse time series using the upper computer software for analysis. This approach facilitates the acquisition of a complete measurement response for the detector. It expedites the identification of any detector issues and enables prompt adjustments such as detector replacement or the fine-tuning of denoising algorithms. Specific details are discussed in Section IV. B.

C. Device Parameters and Evaluation Methods

1. Solution of Neutron Multiplicity Counting Method

The neutron multiplicity counting (NMC) method determines the mass of ^{240}Pu in a sample by formulating and solving measurement equations. These equations rely on the assumption that the sample can be approximated as a point-source model situated at the center of the sample cavity. The measurement equations are derived by solving the multiplicity distribution of the source-event neutrons using a probability-generating function, as shown in Eq. 4, Eq. 5, and Eq. 6. The single rate (S), double rate (D), and triple rate (T) for the NMC method are obtained using the following expressions [2, 4, 29]:

$$S = F\varepsilon M v_{S1} (1 + \alpha) \quad (4)$$

$$D = \frac{F\varepsilon^2 f_d M^2}{2} \left[v_{s2} + \left(\frac{M-1}{v_{i1}-1} \right) v_{s1} (1 + \alpha) v_{i2} \right] \quad (5)$$

$$T = \frac{F\varepsilon^3 f_t M^3}{6} \left\{ v_{s3} + \left(\frac{M-1}{v_{i1}-1} \right) [3v_{s2} v_{i2} + v_{s1} (1 + \alpha) v_{i3}] + 3 \left(\frac{M-1}{v_{i1}-1} \right)^2 v_{s1} (1 + \alpha) v_{i2}^2 \right\} \quad (6)$$

In this equation, in addition to $S/D/T$, F denotes the spontaneous fission rate of the sample, which represents the overall fission level of the sample in units of s^{-1} . ε denotes the detection efficiency of the instrument for neutrons and M is the neutron-leakage multiplication of the sample. The terms v_{sn} and v_{in} denote the first, second, and third reduced moments of spontaneous and induced fission neutron distributions in the sample, respectively. α represents the ratio of the number of (α, n) neutrons produced by a reaction to the number of neutrons produced by fission. f_d and f_t are the double and triple gate fractions, respectively.

Eq. 4, Eq. 5, and Eq. 6 treat the fission-material problem as a parameter-estimation challenge and utilize the moment-estimation method to determine the neutron-leakage multiplication M . Eq. 7 establishes the relationship between M and

the constant coefficients a , b , and c in the equation, which can be expressed as Eq. 8, Eq. 9, and Eq. 10, respectively [4].

$$a + bM + cM^2 + M^3 = 0 \quad (7)$$

$$a = \frac{-6Tv_{s2}(v_{i1} - 1)}{\varepsilon^2 f_t S (v_{s2}v_{i3} - v_{s3}v_{i2})} \quad (8)$$

$$b = \frac{2D[v_{s3}(v_{i1} - 1) - 3v_{s2}v_{i2}]}{\varepsilon f_d S (v_{s2}v_{i3} - v_{s3}v_{i2})} \quad (9)$$

$$c = \frac{6Dv_{s2}v_{i2}}{\varepsilon f_d S (v_{s2}v_{i3} - v_{s3}v_{i2})} - 1 \quad (10)$$

By substituting the neutron-leakage multiplication M of the sample into Eq. 11, the spontaneous fission rate of the sample can be determined.

$$F = \frac{\left[\frac{2D}{\varepsilon f_d} - \frac{M(M-1)v_{i2}S}{v_{i1}-1} \right]}{\varepsilon M^2 v_{s2}} \quad (11)$$

For the plutonium samples, where the fission rate per unit mass of ^{240}Pu is $473.5 \text{ g}^{-1}\text{s}^{-1}$, the equivalent mass of ^{240}Pu in the sample can be expressed using Eq. 12:

$$m_{240} = \frac{F}{473.5} \quad (12)$$

If the isotopic abundance of the plutonium is known, the calculated plutonium mass, denoted by m_c , can be obtained (Eq. 13), where f_n represents the proportion of the different isotopes.

$$m_c = \frac{m_{240}}{2.52 \times \frac{f_{238}}{f_{240}} + 1 + 1.68 \times \frac{f_{242}}{f_{240}}} \quad (13)$$

After calculating the mass (m_c) of ^{240}Pu in the sample, the relative error of the device measurement is determined by comparing it with the actual mass (m_a) of ^{240}Pu in the example using Eq. 14.

$$\Delta = \left| \frac{m_a - m_c}{m_a} \right| \times 100\% \quad (14)$$

However, before employing the NMC method to ascertain the mass of ^{240}Pu in the sample, the parameters such as ε , f_d , and f_t must be calibrated. As f_d and f_t are functions of the detector die-away time (τ), both ε and τ .

2. Detection Efficiency

Because Pu is classified as a military-controlled substance, device calibration often utilizes a ^{252}Cf neutron source with energy levels similar to those of ^{240}Pu fission neutrons. Eq. 15 presents the calculation formula for the detection efficiency.

$$\varepsilon = \frac{n_{\text{detected}}}{n_{\text{emitted}}} \quad (15)$$

Among these parameters, n_{detected} represents the total count rate of the detection array comprising 80 ^3He neutron detectors and n_{emitted} represents the neutron yield of the known neutron source. In practical calibration, a ^{252}Cf source is commonly used to expedite the calibration process. To mitigate systematic errors arising from environmental and electronic circuit influences, the background impact should be considered when calculating n_{detected} . The mean results of multiple measurements are used to reduce the impact of accidental errors. Subsequently, n_{detected} can be expressed using Eq. 16.

$$n_{\text{detected}} = \overline{N}_0 - \overline{N}_b \quad (16)$$

Here, \overline{N}_0 represents the average active count rate obtained from repeated measurements of the instrument when the ^{252}Cf source is at the center of the sample chamber, and \overline{N}_b represents the average background (BG) count rate.

3. Detector Die-away Time

The detector die-away time (τ) is another crucial device parameter, along with the detection efficiency (ε). This signifies the rate at which the neutrons decay from the same fission event in the device.

To ascertain the detector die-away time (τ), one approach involves measuring the double rate (D) of a single neutron source at various 'gate widths' and employing the relationship in Eq. 17. The detector die-away time (τ) can be determined through curve fitting, with D_0 representing the double rate for an infinite gate width.

$$D(GW) = D_0 \times \left[1 - e^{\left(-\frac{(-GW)}{\tau} \right)} \right] \quad (17)$$

The curve-fitting method helps alleviate the computational challenges stemming from the limited selection of gate-width combinations. However, to enhance the precision of the final result, more data points must be measured, and the error in each measurement result contributes to the overall error. Consequently, when employing the curve-fitting method, repeated measurements must be conducted under the same gate-width value to minimize the impact of accidental errors.

After constructing the device, considering a practical scenario, each measurement lasts for 20 s, and the process is repeated 30 times. The measurement results are recorded and the τ values of the device are calibrated according to Eq. 17.

Eq. 18 and Eq. 19 represent the double- and triple-gate fractions, f_d and f_t , respectively. PD represents the pre-delay time in microseconds, and G denotes the gate width in microseconds. The actual values can also be calibrated by using multiple ^{252}Cf sources with different neutron yields.

$$f_d = e^{-\frac{PD}{\tau}} \left(1 - e^{-\frac{G}{\tau}} \right) \quad (18)$$

$$f_t = f_d^2 \quad (19)$$

4. Repeatability of the Measurement Results

In this study, the standard deviation of a single measurement is used to represent the measurement repeatability RSD of the instrument. The calculation formula is shown in Eq. 20, where m_i is the calculated mass of the same sample for different measurements, \bar{m} is the average value of the sample mass, and n is the number of measurements.

$$RSD = \frac{\sqrt{\frac{\sum_{i=1}^n (m_i - \bar{m})^2}{(n-1)}}}{\bar{m}} \times 100\% \quad (20)$$

^{240}Pu samples with various masses were subject to repeated measurements. To align with practical conditions, the individual measurement time was established at 20 s, and the measurement cycle was repeated 30 times. Following these measurements, the RSD values of the results were calculated using Eq. 20, which facilitates the analysis of the repeatability of the device-measurement outcomes.

III. DESIGN PARAMETER DETERMINATION AND DEVICE CONSTRUCTION

A. Simulation and parameter determination

Based on the design plan, the ^3He neutron detector-array system comprises 80 detectors arranged in a circular pattern around the central axis of the sample chamber. The detectors are organized into four rings, with each ring containing 19, 25, 18, and 18 detectors. Furthermore, as determined in Section II.A, the effective length of ^3He and thickness of the graphite reflective layer atop the plug are indispensable factors that have a profound impact on the capacity to discern efficiency. To achieve a detection efficiency above 40 % at the lowest cost, Monte Carlo software is used to simulate and analyze various factors that affect the detection efficiency. This meticulous procedure is undertaken with the sole aim of deducing the optimal values of the effective length of ^3He and the thickness of the graphite reflective layer. The chosen simulation software is MCNP, with various nuclear reaction cross-sections referenced from the NDF/B-VIII.0 nuclear database [30, 31].

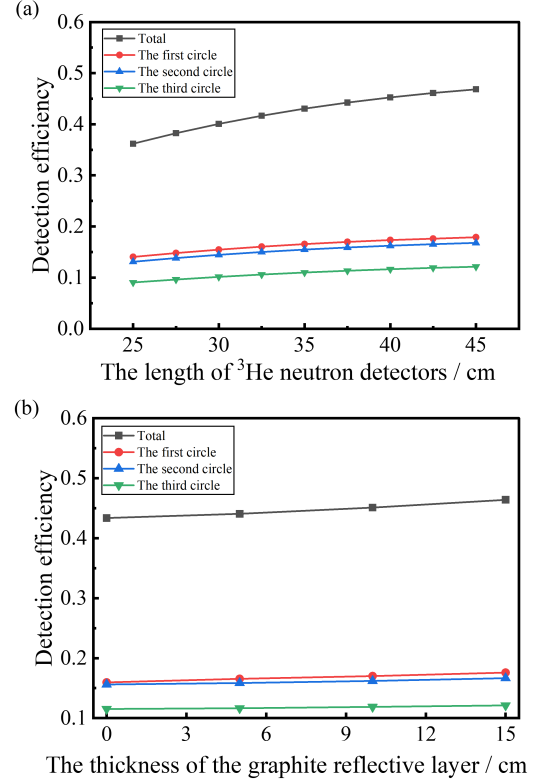


Fig. 3. Detection efficiency of the device varying with the effective length of the detector. ((a) Influence of effective length of ^3He neutron detectors; (b) influence of graphite reflective layer)

During the simulation, a ^{252}Cf point source is strategically placed at the focal point within the confines of the sample chamber. The sample chamber is maintained at a height of 20 cm, and the effective length fluctuates between 25 and 45 cm. Fig. 3 (a) illustrates the relationship between the detection efficiency of the device and effective length of the detector. From Fig. 3 (a), the detection efficiency increases with an appropriate sensor size. When the detector's size is 30 cm, the detection efficiency surpasses 40 %. Therefore, a ^3He neutron detector with an effective length of 30 cm proves to be the most cost-effective and efficient choice for a detection array.

Considering the distribution of the ^3He neutron detectors, the thickness of the graphite reflective layer is progressively increased from 0 to 15 cm. Fig. 3 (b) presents the overall detection efficiency of the device and trend of the detection efficiency per ring as the thickness of the graphite reflective layer increases. The results indicate that the detection efficiency increases with the thickness of the graphite reflector. Owing to the space limitations in the sample cavity, the thickness of the graphite reflector in this study is set to 15 cm.

Each ^3He neutron detector has a diameter of 2.54 cm and an effective gas length of 30 cm. The upper segment incorporates electronic circuits extending approximately 15 cm in length, and the gas pressure is meticulously regulated at 4

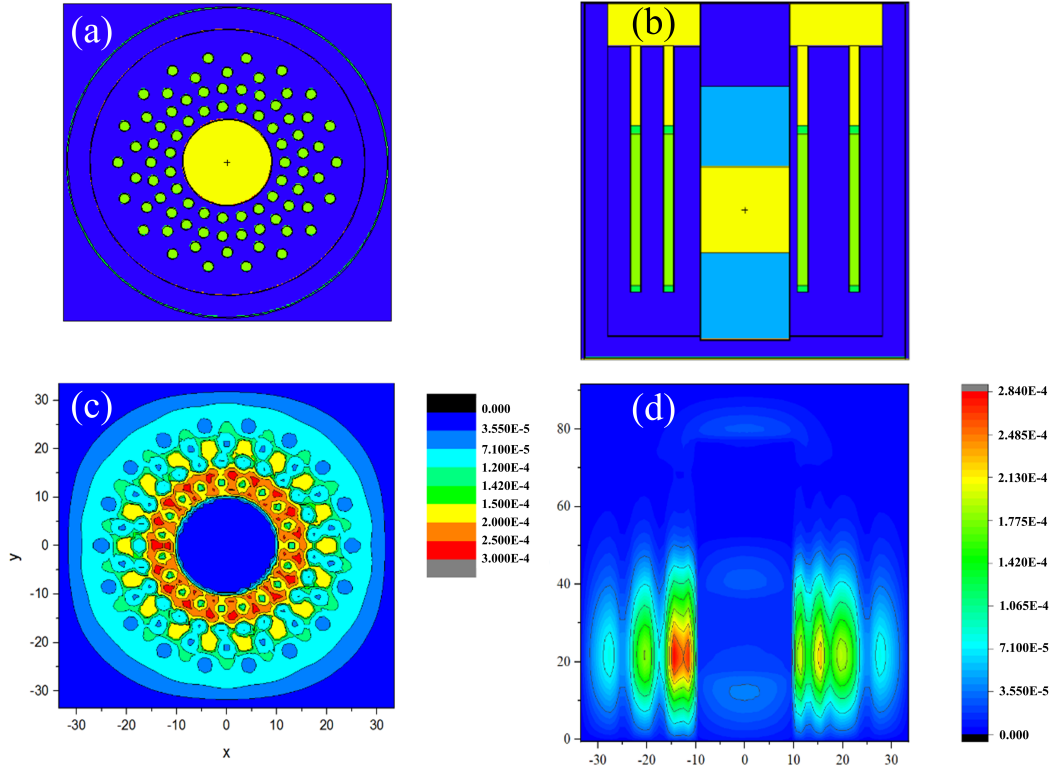


Fig. 4. Model diagram of multiplicity devices established in MCNP.((a): XY cross-sectional view of MCNP model; (b): XZ cross-sectional view of MCNP model; (c): thermal neutron distribution map of XY cross section (d): thermal neutron distribution map of XZ cross section)

atm. The summit plug comprises a stratum of graphite with a thickness of 15 cm. The lower region extends from the base of the sample chamber to the bottom of the device. The comprehensive dimensions of the device encompass a height of 82.7 cm and length and width dimensions of 74.2 cm. The model schematic is constructed using MCNP based on the aforementioned information and the device-design diagram in Fig. 1, as shown in Fig. 4 (a) and (b).

Similarly, a ^{252}Cf source was positioned at the focal point within the confines of the sample chamber, and the dispersion of thermal neutrons on the axial and radial cross-sections at the central coordinates of the sample chamber was meticulously documented. Fig. 4 (c) and Fig. 4(d) illustrate the results of the thermal neutron distribution at various positions within the device, as simulated using MCNP.

Referring to Fig. 4 (c) and (d), because of the presence of moderators, fast neutrons rapidly lose energy and transform into thermal neutrons. Owing to the absorption of thermal neutrons by ^3He gas in the neutron detectors, the thermal neutrons in the device achieve a sufficiently low level to be deemed inconsequential after they traverse the ultimate ring of the detectors. The incorporation of the Cd layer renders thermal neutrons within the sample chamber practically negligible. Simultaneously, the Cd veneer on the outer surface of the initially decelerating structure absorbs residual thermal neutrons. In the outermost tier of the apparatus, thermal neu-

trons are nearly nonexistent, thereby attesting to the extraordinary proficiency of the device in neutron shielding.

The simulation conducted a preliminary calculation of the device detection efficiency, yielding a value of 42.10 % based on Eq. 15. According to Eq. 17, the detector die-away time of the device was computed as $54.66 \mu\text{s}$. These data serve as references for the subsequent calibration of the device.

B. Passive neutron multiplicity device construction

Upon determining the optimal parameters of the device, the device was constructed and assembled. The overall structure of the device is shown in Fig. 5 (a), and Fig. 5 (b) shows the upper computer-analysis software that supports the multiplicity device. Fig. 5 (c) shows the internal electronic circuitry of the device, where each ^3He neutron detector in FH-NCM/S1 is connected to a preamplifier, totaling 80 channels positioned directly above the ^3He neutron detector. Three circuit boards are employed to collect information from the 80 channels of the ^3He neutron detector, and the circuit board is illustrated in Fig 5 (e). Each channel is powered independently to simplify maintenance and replacement.

The signal-acquisition and transmission module comprises several key components: a ^3He neutron detector unit, detector power supply, signal-adaptor board (Fig. 5 (e)), and signal-acquisition board (Fig. 5 (d)). The ^3He neutron detector unit

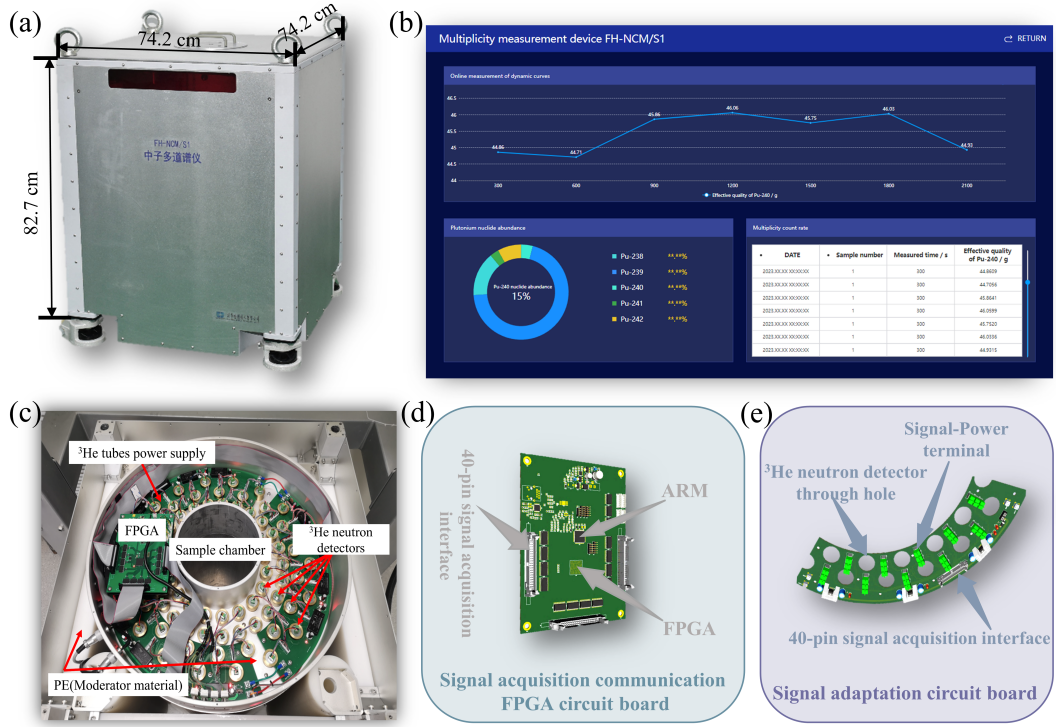


Fig. 5. Overall and internal structural details of FH-NCM/S1 and the upper computer software. ((a) Overall appearance of the device; (b) upper computer-software measurement interface; (c) device electronics-circuit part; (d) FPGA circuit board; (e) signal-adaptation circuit board).

requires a power-supply voltage of 12 Vdc, which is achieved using an independent high-voltage power-supply module. In addition, the unit incorporates signal amplification, shaping, and a comparator output circuit. The neutron-detection signal undergoes shaping and is output as a TTL-level negative logic signal, ensuring swift equipment response, even over long transmission lines.

The chassis incorporates three signal-adaptation circuit boards, as shown in Fig. 5 (e). Each signal-adaptation circuit board can provide 12 Vdc @ 500 mA output power, supporting up to 30 ³He neutron-detector power channels. They are linked to the FPGA through a 40-pin terminal to scan and collect the output signals.

The signal-acquisition board receives signals from the three-channel adapter board, overseeing the input voltage of the adapter board and the 12 V power supply voltage of the nine-channel ³He neutron detector group. The interface-conversion chip transforms the pulse signals from the 80-channel ³He neutron detectors, which are then collected by the FPGA. The FPGA concurrently monitors and conducts analytical calculations for the counting status of the 80-channel ³He neutron detectors. The processed data output results are transmitted to the host-computer software through a field bus or 10/100 Mbps network port. Following the processing and calculation of the data using the upper computer software, the results are displayed in real time on the software interface, as illustrated in Fig. 5 (b).

IV. DISCUSSION ON DEVICE CALIBRATION AND MEASUREMENT RESULTS

A. Calibration Results of FH-NCM/S1

1. Detection Efficiency

Suitable measurement parameters are configured for the actual tests. The neutron yield of the ²⁵²Cf source utilized in the measurement is $2.78 \times 10^6 \text{ s}^{-1}$. The source, including the background and known neutron yield, is measured for 300 s six times. The total count of the ³He detection array is recorded for each occasion, and the overall detection efficiency of the device is calculated using Eq. 15 and Eq. 16.

After constructing the device, appropriate measurement parameters are set to consecutively measure the background and ²⁵²Cf source with a known neutron yield six times, each lasting 300 s. The counting rate of the ³He detection array is recorded for each occasion. The measured \bar{N}_0 is 1197267.3 and \bar{N}_b is 1.5. The average count rate after deducting the background is $1.20 \times 10^6 \text{ s}^{-1}$. Using Eq. 15 and Eq. 16, the detection efficiency (ϵ) is calculated to be 43.07 %, which is close to 42.10 %, which is obtained from the simulation.

2. Detector Die-away Time

In the actual test, each measurement lasts for 20 s, and the measurement is repeated 30 times. The measurement results of the average value of S and double-rate D under different gate widths are recorded. Eq. 17 is used to fit the data obtained by using a curve-fitting method. The curve of Eq. 17 is plotted, as shown in Fig. 7 (a). The fitting result for the value is $55.79 \mu\text{s}$, which is close to $54.66 \mu\text{s}$, obtained from the simulation.

3. Sample Quantitative Results and Relative Error

Owing to the insufficient availability of ^{252}Cf sources for the measurement, the feasibility of the device was directly verified by comparing the measurement results of nine different standard plutonium oxide samples (with ^{240}Pu masses ranging from 0.1 g to 54.5 g) using the FH-NCM/S1 device and PSMC combined with JSR-15. These cylindrical plutonium oxide samples have the same density and encapsulation method, and the abundances of the different isotopes are consistent, with differences only in the diameter and height. The shift-register analysis mode of the FH-NCM/S1 device is used for the measurement and compared with the measurement mode of JSR-15. Each sample is measured for 300 s in a single measurement, which is repeated three times. Standard plutonium samples are measured and quantitatively analyzed using FH-NCM/S1 and PSMC devices.

The relationship between the double rates and equivalent mass of ^{240}Pu is shown in Fig. 7 (b). When the measuring materials are the same, the fitting curve of the double rate of the new device exhibits a shape similar to that of the PSMC device. However, the two curves do not completely overlap. According to the definition of the double rate (refer to Eq. 5), this discrepancy arises because it is influenced not only by the measurement material, but also by the detection efficiency of the device (ε) and double-gate fraction (f_d).

To further evaluate the effectiveness of the device, according to Eq. 5, after eliminating the impact of the detection efficiency (ε) and double-gate fraction (f_d), the correct double rate (D_c) obtained when two devices measure the same sample can be approximated as only related to the sample itself (Eq. 21). Therefore, the corresponding measurement results for the two devices for the same sample should exhibit a proportional relationship ($D_{c_PSMC} = D_{c_FH-NCM/S1}$).

$$D_c = \frac{D}{\varepsilon^2 f_d} = \frac{FM^2}{2} \left[v_{s2} + \left(\frac{M-1}{v_{i1}-1} \right) v_{s1} (1 + \alpha) v_{i2} \right] \quad (21)$$

The pre-delay times for FH-NCM/S1 and PSMC are set to $3 \mu\text{s}$, the gate width is set to $64 \mu\text{s}$ [28], and the long delay time is set to 2 ms. The double-gate fractions (f_d) of FH-NCM/S1 are calculated using Eq. 18 and the two parameters required for Eq. 21 and the die-away time are listed in Table 1.

Table 1. Parameters for measuring FH-NCM/S1 and PSMC

Parameters	Value	
	FH/NCM-S1	PSMC
Detection Efficiency	0.431	0.533
Double-Gate Fraction	0.6467	0.6279
Detector Die-away Time	$55.79 \mu\text{s}$	$49.10 \mu\text{s}$

Fig. 7 (c) shows that the linearity of the double-rate (D) measured by the two devices for the same sample is exceptional, indicating that the new device is capable of detecting Pu. Three potential sources of error exist between the two devices. First, errors may exist in the detection efficiency (ε) and double-gate fraction (f_d) of the device used to correct D_c . Second, the influence of dead time during the sample-measurement process cannot be ignored when the device measures a large sample. Lastly, measurement errors may occur, particularly when the sample has a low number of fission neutrons.

Samples No.1, No.2, and No.3, with ^{240}Pu effective masses of 0.54 g, 27.23 g, and 45.50 g, respectively, are measured using a single measurement of 20 s and 30 cycles. After 30 measurement cycles, the calculated masses (m_c) of ^{240}Pu in the samples are calculated. Based on Eq. 11, Eq. 12, and Eq. 13, the results of the quantitative and error calculations for the three samples with similar appearances and different qualities are presented in Table 2. As shown in Table 2, the relative error between the measurement and calculation of the device is less than 5 %, which satisfies the measurement requirements of the sample.

Table 2. Measurement results and relative error of samples

Measurement ID	Sample 1		Sample 2		Sample 3	
	m_c / g	$\Delta / \%$	m_c / g	$\Delta / \%$	m_c / g	$\Delta / \%$
1	44.860	1.40	27.920	2.58	0.531	1.65
2	44.706	1.75	27.063	0.57	0.557	3.13
3	45.864	0.80	26.371	3.11	0.547	1.24
4	46.060	1.23	27.755	1.97	0.533	1.33
5	45.752	0.55	26.828	1.44	0.562	4.11

4. The Repeatability of the Measurement Results

The effective mass of ^{240}Pu , obtained by measuring the same plutonium sample, is shown in Fig. 7 (d) and Fig. 7 (e) with a single measurement time of 20 s (a small measurement cycle). The relative standard deviation (RSD) of the calculation results is determined based on Eq. 21. The RSD value of the small-mass sample (sample No.3) measured using the device is 7.23 %, and the RSD value of the large-mass sample (sample No.1) is 9.87 %. The repeatability of the 20 s measurement is good, thereby satisfying the production-measurement requirements.

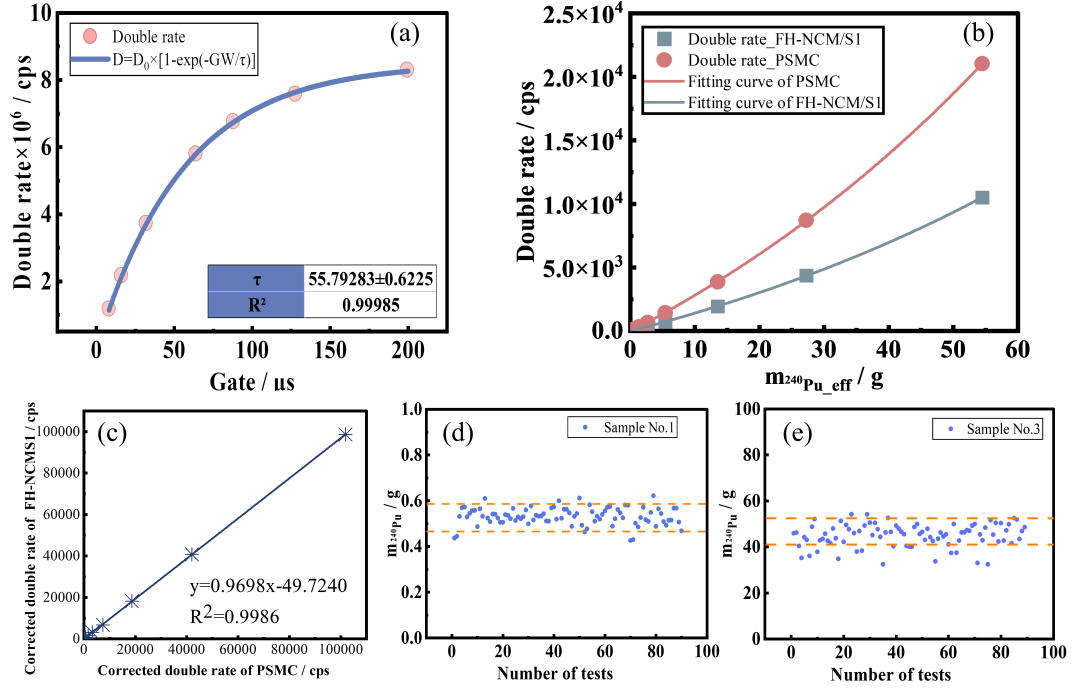


Fig. 6. Actual measurement results of FH-NCM/S1 ((a) Die-away-time fitting curve; (b) measurement curves of two devices for the same sample; (c) comparison of measurement curves after removing the influence of parameters; (d) multiple measurement curves of sample 1; (e) multiple measurement curves of sample 3).

B. Comparison of different analysis methods

To test the accuracy of the transmission information of the pulse-position timestamp mode of the device, both shift-register analysis and pulse-position timestamp modes are employed to measure the same unknown sample. After measuring for 300 s in each mode, the measured $S/D/T$ and normalized distributions of $R+A$ and A are recorded. The partial fragments of the pulse-sequence time spectrum recovered using this software are shown in Fig. 6. The minimum resolution for Δt in this mode is 20 ns.

The distribution results recovered from the pulse-position timestamp mode and shift-register analysis mode using the same measurement parameters (pre-delay time is $3 \mu s$, gate width is $64 \mu s$, and long-delay time is 2 ms) are shown in Table 3. For clarity, the data in Table 3 has been normalized. The $S/D/T$ values obtained by the two modes are 3119.20, 230.00, and 19.99 (pulse-position timestamp mode) and 3177.80, 230.20, and 17.11 (shift-register analysis mode), in cps.

The CORREL function is used to compute the correlation between the distribution results presented in Table 3, as expressed in Eq. 22, to evaluate the coherence of the measurement outcomes across dual modalities. Within Eq. 22, $C_{comprehensive}$ is utilized as a parameter to gauge the uniformity of the two measurement methodologies, featuring values within the -1—1 range. A proximity to 1 signifies heightened

Table 3. Distribution of normalized information of $(R+A)$ and (A) collected by two methods

n	Pulse position timestamp mode		Shift Register Analysis Mode	
	P1(n)	Q1(n)	P2(n)	Q2(n)
0	7.27E-01	7.80E-01	7.27E-01	7.80E-01
1	2.21E-01	1.86E-01	2.22E-01	1.87E-01
2	4.40E-02	2.90E-02	4.36E-02	2.83E-02
3	6.35E-03	3.85E-03	6.09E-03	3.53E-03
4	9.62E-04	7.69E-04	1.03E-03	7.70E-04
5	1.92E-04	0.00E+00	0.00E+00	0.00E+00

congruity in the measurement results between the two modalities. ‘a’ and ‘b’ serve as invariable coefficients symbolizing the weights attributed to the correlation of the $R+A$ and A statistical data distributions, both set to 0.5. P_n and Q_n signify the normalized distribution probabilities of $R+A$ and A under the two modalities, respectively, as listed in Table 3.

$$\begin{aligned}
 C_{comprehensive} &= a \text{Correl}(P1, P2) + b \text{Correl}(Q1, Q2) \\
 &= a \frac{\sum (P1 - \bar{P1})(P2 - \bar{P2})}{\sqrt{\sum (P1 - \bar{P1})^2 \sum (P2 - \bar{P2})^2}} \\
 &\quad + b \frac{\sum (Q1 - \bar{Q1})(Q2 - \bar{Q2})}{\sqrt{\sum (Q1 - \bar{Q1})^2 \sum (Q2 - \bar{Q2})^2}}
 \end{aligned} \tag{22}$$

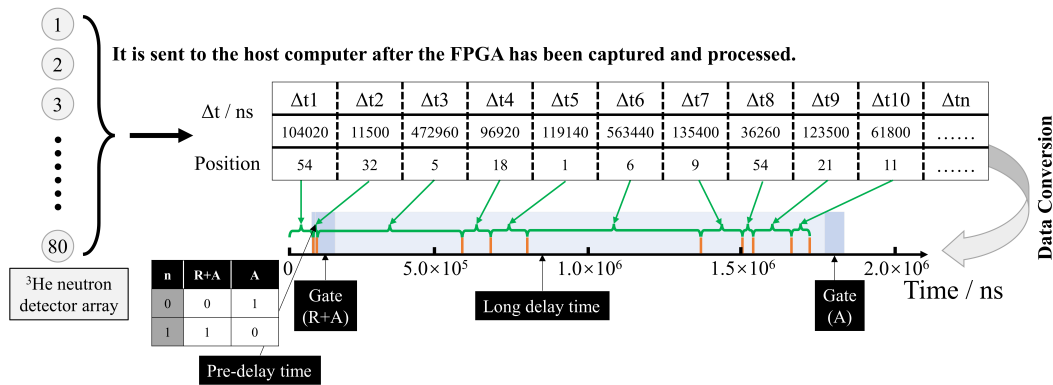


Fig. 7. Actual measurement results of FH-NCM/S1 (pulse-position timestamp mode).

According to Eq. 22, the calculated value for $C_{\text{comprehensive}}$ is 0.999, demonstrating a striking similarity between the distributions obtained using the two methodologies. This confirms the viability of multiplicity data measurements using the pulse-position timestamp method employed by the device. Moreover, adopting this approach to collect pulse signals facilitates convenient storage for offline measurements, data research, and analysis, thereby significantly enhancing the efficiency of data storage and organization.

V. CONCLUSION

This study investigates the intricacies of simulation optimization, device fabrication, parameter calibration, and the nuanced evaluation of a novel passive neutron multiplicity apparatus, FH-NCM/S1, which is based on the neutron multiplicity principle. The refined apparatus comprises a quartet of concentric rings housing ^3He neutron detectors. Each of the four rings accommodates 19, 25, 18, and 18 detectors, which are meticulously arrayed symmetrically around the central cavity. By harnessing the computational process of the Monte Carlo program MCNP, the optimization process entails fine-tuning the effective length of the ^3He neutron detector and the dimensions of the graphite moderator. The outcome indicates that the optimal length for the sensor is 30 cm, and the detection efficiency can exceed 40 % with a moderator thickness of 15 cm.

Upon completion of the device setup, calibration was performed using a ^{252}Cf source to determine the detection efficiency and die-away time, resulting in 43.07 % and 55.79 μs , respectively. Subsequently, the shift-register analysis mode of the device was employed to measure nine plutonium oxide standards. After comparing the obtained dual counting rate (D) with the results obtained using the PSMC and JSR-15 combination, a modified dual counting rate (D_c) was proposed, validating the rationality of the shift-register analysis mode data-processing and solution methods. The performance of the device was demonstrated by measuring three

standard plutonium samples using FH-NCM/S1 with a single measurement time of 20 s and fluctuations between consecutive measurements below 10 %. After 30 measurement cycles, the relative error for ^{240}Pu mass measurement was less than 5 %, which meets commercial-application conditions.

Finally, by comparing the measurements of the same plutonium-containing sample obtained with FH-NCM/S1 operating in both the shift-register analysis mode and pulse-position timestamp mode, the consistency of the results between the two operational modes was verified. This study provides valuable information for the subsequent development, design, and performance assessment of passive neutron multiplicity measurement devices and offers meaningful guidance for future endeavors in the field.

VI. CONTRIBUTIONS STATEMENT

All authors contributed to the conception and design of this study. Material preparation, data collection, and analysis were performed by Yan Zhang, Hao-Ran Zhang, Ren-Bo Wang, Ming-Yu Li, Rui Chen, Hai-Tao Wang, Xiang-Ting Meng, Shu-Min Zhou, and Bin Tang. Yan Zhang and Hao-Ran Zhang wrote the first draft of the manuscript, and all authors commented on previous versions of the manuscript. All the authors have read and approved the final version of the manuscript.

VII. CONFLICT OF INTEREST

The authors declare that they have no competing interests.

VIII. DATA AVAILABILITY STATEMENT

The data supporting the findings of this study are openly available from the Science Data Bank at <https://doi.org/10.57760/sciencedb.13183>.

- [1] A. Asghari, S. Dazeley, A. Bernstein, A plutonium mass uncertainty assessment using a cherenkov-based neutron multiplicity water detector. *IEEE T. Nucl. Sci.* **67**, 2431–2438 (2020). doi: [10.1109/TNS.2020.3027668](https://doi.org/10.1109/TNS.2020.3027668)
- [2] L.G. Chen, G. Jian, K. Wang et al., Variance analysis for passive neutron multiplicity counting. *Nucl. Sci. Tech.* **26**, 2 (2015). doi: [10.13538/j.1001-8042/nst.26.020402](https://doi.org/10.13538/j.1001-8042/nst.26.020402)
- [3] C. Roecker, A. Bernstein, P. Marleau et al., Measurement of high-energy neutron flux above ground utilizing a spallation based multiplicity technique. *IEEE T. Nucl. Sci.* **63**, 2823–2829 (2016). doi: [10.1109/TNS.2016.2628644](https://doi.org/10.1109/TNS.2016.2628644)
- [4] D.G. Langner, J.E. Stewart, M.M. Pickrell et al., Application Guide to Neutron Multiplicity Counting. Los Alamos National Laboratory. **Los Alamos**, NM (1998). doi: [10.2172/1679](https://doi.org/10.2172/1679)
- [5] M.C. Qiu, W.B. Jia, D.Q. Hei et al., Digital stabilization algorithm for the gamma spectra of scintillator detectors in PGNA. *IEEE T. Nucl. Sci.* **69**, 113–117 (2022). doi: [10.1109/TNS.2021.3139391](https://doi.org/10.1109/TNS.2021.3139391)
- [6] J.T. Li, W.B. Jia, D.Q. Hei et al., Design of the explosion-proof detection integrated system based on pgnaa technology. *J. Radioanal. Nucl. Ch.* **322**, 1719–1728 (2019). doi: [10.1007/s10967-019-06837-7](https://doi.org/10.1007/s10967-019-06837-7)
- [7] Y. Yahagi, H. Yamaguchi, E. Ibe et al., A novel feature of neutron-induced multi-cell upsets in 130 and 180 nm srams. *IEEE T. Nucl. Sci.* **54**, 1030–1036 (2007). doi: [10.1109/TNS.2007.897066](https://doi.org/10.1109/TNS.2007.897066)
- [8] Y.C. Yan, M.Z. Liu, X.Y. Li et al., Improved Cohen-Sutherland algorithm for TGS transmission imaging. *Nucl. Sci. Tech.* **34** (06), 206–217 (2023). doi: [10.1007/s41365-023-01238-8](https://doi.org/10.1007/s41365-023-01238-8)
- [9] A.Y. Sun, W.B. Jia, J.T. Li et al., Method for accurate position detection of landmine based on PGNA technology. *J. Radioanal. Nucl. Ch.* **320**, 323–328 (2019). doi: [10.1007/s10967-019-06498-6](https://doi.org/10.1007/s10967-019-06498-6)
- [10] C.C. Cowles, R.S. Behling, G.R. Imel et al., Effects of correlated and uncorrelated gamma rays on neutron multiplicity counting. *IEEE T. Nucl. Sci.* **64**, 1865–1870 (2017). doi: [10.1109/TNS.2017.2667407](https://doi.org/10.1109/TNS.2017.2667407)
- [11] J. Mattingly, Computation of neutron multiplicity statistics using deterministic transport. *IEEE T. Nucl. Sci.* **59**, 314–322 (2012). doi: [10.1109/TNS.2012.2185060](https://doi.org/10.1109/TNS.2012.2185060)
- [12] M. C. Tweardy, S. McConchie, J. P. Hayward et al., A point kinetics model for estimating neutron multiplication of bare uranium metal in tagged neutron measurements. *IEEE T. Nucl. Sci.* **64**, 1963–1969 (2017). doi: [10.1016/j.advwatres.2008.01.022](https://doi.org/10.1016/j.advwatres.2008.01.022)
- [13] L. Steinbock, Transmission tomography of nuclear fuel pins and bundles with an electronic line camera system. *J. Nucl. Mater.* **178**, 277–383 (2008). doi: [10.1016/j.jnucmat.2008.01.022](https://doi.org/10.1016/j.jnucmat.2008.01.022)
- [14] B. Fraïsse, G. Béliet, V. Méot et al., Complete neutron-multiplicity distributions in fast-neutron-induced fission. *Phys. Rev. C* **108**, 014610 (2023). doi: <https://doi.org/10.1103/PhysRevC.108.014610>
- [15] H.Y. Bai, Z.H. Xiong, D.S. Zhao et al., A method of obtaining the neutron multiplicity distribution online based on the list-mode data acquisition. *Nucl. Instrum. Meth. A* **1056**, 168652(2023). doi: [10.1016/J.NIMA.2023.168652](https://doi.org/10.1016/J.NIMA.2023.168652)
- [16] P. Humbert, Neutron Multiplicity Counting Distribution Reconstruction from Moments Using Meixner Polynomial Expansion and N-Forked Branching Approximations. *Nucl. Sci. Eng.* **197**, 2356–2372(2023).doi: [10.1080/00295639.2022.2162304](https://doi.org/10.1080/00295639.2022.2162304)
- [17] M. Fang, J. Lacy, A. Athanasiades et al., Boron coated straw-based neutron multiplicity counter for neutron interrogation of triso fueled pebbles. *Ann. Nucl. Energy* **187**, 109794(2023). doi: [10.1016/J.ANUCENE.2023.109794](https://doi.org/10.1016/J.ANUCENE.2023.109794)
- [18] S. Bürger, S.D. Balsley, S. Baumann et al., Uranium and plutonium analysis of nuclear material samples by multi-collector thermal ionisation mass spectrometry: Quality control, measurement uncertainty, and metrological traceability. *Int. J. Mass. Spectrom.* **311**, 40–50 (2012). doi: [10.1016/j.ijms.2011.11.016](https://doi.org/10.1016/j.ijms.2011.11.016)
- [19] K. Ogren, D. Henzlova, J. Longo et al., Demonstration of INCC6 for advanced list-mode data acquisition and analysis using ALMM. *Nucl. Instrum. Meth. A* **1058**, 168797 (2024). doi: [10.1016/J.NIMA.2023.168797](https://doi.org/10.1016/J.NIMA.2023.168797)
- [20] Z.W. Fu, Y.K. Heng, S.J. Gu et al., Efficiency-determined method for thermal neutron detection with inorganic scintillator. *Nucl. Sci. Tech.* **24**, 040205 (2013). doi: [10.13538/j.1001-8042/nst.2013.04.010](https://doi.org/10.13538/j.1001-8042/nst.2013.04.010)
- [21] Y.T. Li, W.P. Lin, B.S. Gao et al., Development of a low-background neutron detector array. *Nucl. Sci. Tech.* **33**, 41 (2022). doi: [10.1007/s41365-022-01030-0](https://doi.org/10.1007/s41365-022-01030-0)
- [22] E. Aboud, S. Ahn, G.V. Rogachev et al., Modular next generation fast neutron detector for portal monitoring. *Nucl. Sci. Tech.* **33**, 13 (2022). doi: [10.1007/s41365-022-00990-7](https://doi.org/10.1007/s41365-022-00990-7)
- [23] T.P. Peng, X.B. Zhu, H.Q. Yang et al., Sensitivity of a new-developed neutron detector. *Nucl. Sci. Tech.* **16**, 40–42 (2005).
- [24] Q.Q. Pan, Q.F. Zhao, L.J. Wang et al, Rapid diagnostic method for transplutonium isotope production in high flux reactors. *Nucl. Sci. Tech.* **34**, 44 (2023). doi: [10.1007/s41365-023-01185-4](https://doi.org/10.1007/s41365-023-01185-4)
- [25] X.C. Zhao, Y. Zou, R. Yan et al., Analysis of burnup performance and temperature coefficient for a small modular molten-salt reactor started with plutonium. *Nucl. Sci. Tech.* **26**, 60–61 (2015). doi: [10.1007/s41365-022-01155-2](https://doi.org/10.1007/s41365-022-01155-2)
- [26] S.T. Xiao, L. Li, G.A. Ye et al., An improvement in APOR process I-uranium/plutonium separation process. *Nucl. Sci. Tech.* **26**, 040605 (2015). doi: [10.13538/j.1001-8042/nst.26.040605](https://doi.org/10.13538/j.1001-8042/nst.26.040605)
- [27] H.H. Ding, F. Gao, C.B. Lu et al., Gamma ray multiplicity of a 240Pu solid sphere simulated by JMCT. *Nucl. Sci. Tech.* **33**, 53 (2022). doi: [10.1007/s41365-022-01043-9](https://doi.org/10.1007/s41365-022-01043-9)
- [28] C. Stephen, G.E. Louise and A.S. Melissa, Optimal gate-width setting for passive neutron multiplicity counting. Los Alamos National Laboratory. **LA-UR-10-04453**, 2010.
- [29] L.A. Carrillo, N. Ensslin, M.S. Krick et al., Uncertainty analysis for determination of plutonium mass by neutron multiplicity. Los Alamos National Laboratory. **LA-UR-98-3044**, 1998.
- [30] D.B. Pelowitz, MCNPX user's manual version 2.5.0. Los Alamos National Laboratory. **LA-CP-05-0369**, 2005.
- [31] X. G. Tuo, J.B. Yang, K.L. Mu et al., Monte Carlo simulation to key parameters of a compensated neutron logger. *Nucl. Sci. Tech.* **20**, 359–362 (2009). doi: [10.1109/CLEOE-EQEC.2009.5194697](https://doi.org/10.1109/CLEOE-EQEC.2009.5194697)